nature communications

Article

https://doi.org/10.1038/s41467-025-67561-3

Doping-induced magnetic phase transition enables all-electrical spin control in CrSBr

Received: 6 July 2025

Accepted: 3 December 2025

Published online: 19 December 2025

Check for updates

Guorui Zhao[1,2], Yibin Zhao[1,2], Yu Zhang[3], Kunlin Yang[1,2], Zejing Guo[1,2], Jiaqi Liu[1,2], Tuoyu Zhao[1,2], Kun Yan[4], Xiaobin Chen[4], Qi Li[5], Yingchun Cheng[6], Cheng Zhang[1,2], Zhe Wang[7], Yi Liu[8], Jianting Ye[9], Jia-Wei Mei[10] ✉, Zhe Yuan[1,11] ✉ & Wu Shi[1,2] ✉

Van der Waals antiferromagnetic semiconductors are promising platforms for energy-efficient two-dimensional spintronics. However, their intrinsic spin degeneracy and the difficulty of achieving electrical spin control pose major challenges for practical device implementation. Here, we present a distinct spintronic platform based on an antiferromagnetic semiconductor CrSBr, in which carrier doping induced by gate-controlled intercalation drives a reversible, zero-field antiferromagnetic to ferromagnetic phase transition, enabling direct and full electrical control of both magnetic order and spin polarization. Exploiting this transition, we engineer CrSBr/graphene heterostructures that leverage interfacial charge transfer to spatially pattern magnetic phases, resulting in lateral spin valves with gate-controlled spin polarization reversal, all without ferromagnetic contacts. Crucially, this mechanism also enables electrical switching of magnetic order via spin-transfer torque at ultralow current densities ($<10^3$ A/cm^2), demonstrating its efficiency and device compatibility. These findings open a new paradigm for reconfigurable, all-electrical spintronic systems based on van der Waals antiferromagnetic semiconductors.

The pursuit of electrical control over magnetic order and spin polarization in quantum materials stands at the forefront of condensed matter physics, offering a pathway to energy-efficient spintronic devices for information storage and processing[1–4]. Layered van der Waals (vdW) magnets have recently emerged as a highly promising platform due to their gate-tunable magnetic states and tailorable interlayer interactions[5–12]. Among them, A-type collinear antiferromagnets are of particular interest for their unique combination of intralayer ferromagnetism and interlayer antiferromagnetic (AFM) coupling, which results in layer-locked spin-polarized bands with zero net magnetization[13–15]. Recent work has demonstrated that electric-field-induced symmetry breaking in even-layer $CrPS_4$ can spin-polarize

[1]State Key Laboratory of Surface Physics and Institute for Nanoelectronic Devices and Quantum Computing, Fudan University, Shanghai, China. [2]Zhangjiang Fudan International Innovation Center, Fudan University, Shanghai, China. [3]Center for Advanced Quantum Studies and School of Physics and Astronomy, Beijing Normal University, Beijing, China. [4]School of Science, State Key Laboratory on Tunable Laser Technology and Ministry of Industry & Information Technology Key Lab of Micro-Nano Optoelectronic Information System, Harbin Institute of Technology, Shenzhen, China. [5]Key Laboratory of Flexible Electronics & Institute of Advanced Materials, Jiangsu National Synergetic Innovation Center for Advanced Materials, Nanjing Tech University, Nanjing, China. [6]State Key Lab of Metastable Materials Science & Technology and Key Laboratory for Microstructure Material Physics of Hebei Province, School of Science, Yanshan University, Qinhuangdao, China. [7]MOE Key Laboratory for Nonequilibrium Synthesis and Modulation of Condensed Matter, School of Physics, Xi'an Jiaotong University, Xi'an, China. [8]Institute for Quantum Science and Technology, Department of Physics, Shanghai University, Shanghai, China. [9]Device Physics of Complex Materials, Zernike Institute for Advanced Materials, University of Groningen, Groningen, The Netherlands. [10]State Key Laboratory of Quantum Functional Materials, Department of Physics, and Guangdong Basic Research Center of Excellence for Quantum Science, Southern University of Science and Technology, Shenzhen, China. [11]Interdisciplinary Center for Theoretical Physics and Information Sciences, Fudan University, Shanghai, China. ✉e-mail: meijw@sustech.edu.cn; yuanz@fudan.edu.cn; shiwu@fudan.edu.cn

conduction bands[13,14], although this method preserves the interlayer AFM order. A more effective form of spin control involves directly manipulating the coupling between layers to drive an interlayer AFM-to-ferromagnetic (FM) transition, where the phase change can drastically alter the global magnetic state. However, realizing such deterministic spin control at zero magnetic field via the AFM-to-FM transition remains experimentally challenging[9–11,16–18].

Carrier doping offers a powerful alternative for tuning magnetism and unlocking emergent quantum states, as illustrated in colossal magnetoresistance (MR) systems[19] and high-temperature superconductors[20]. Electrical control of carrier concentration, in particular, has been implemented to modulate magnetic order[8] via spin-charge coupling controlled by gating. A vdW semiconductor CrSBr (Supplementary Note 1 and Fig. S1), showing A-type AFM order (Fig. 1a), can host more dramatic doping responses: due to its weak interlayer coupling and strong charge-spin correlations[16,21,22], doping CrSBr can directly induce both magnetic ordering and spin polarization. Theoretical calculations reveal a stark contrast between AFM and FM configurations in its spin-resolved density of states (DOS) (Fig. 1a, b): the AFM state exhibits spin degeneracy (net polarization $P = 0$), whereas the FM phase shows near-complete spin polarization at the conduction and valence band edges. Crucially, calculations of the AFM-FM energy difference (Fig. 1c and Supplementary Fig. S2) demonstrate that carrier doping stabilizes the FM state at experimentally accessible densities (10^{12} ~ 10^{14} cm^2), aligning with previous predictions[21], thus establishing carrier doping as an effective mechanism for modulating interlayer magnetic order and spin polarization.

Guided by these insights, we demonstrate in situ electrical control of both magnetic order and spin polarization in CrSBr at zero external magnetic field. First, we use ionic gating to drive a reversible AFM-to-FM transition, manifested in distinct hysteretic MR signatures. Second, leveraging local interfacial charge transfer from graphene (Gr) contacts, we spatially modulate the magnetic order to form a lateral spin-valve configuration with gate-tunable spin polarization (Fig. 1d). Finally, we achieve electrical modulation of magnetic order in the lateral CrSBr channel via spin-transfer torque (STT) at ultralow current densities. These results together establish CrSBr as a versatile platform for all-electrical spintronics, enabling integrated control of magnetism and spins without relying on FM contacts[23–26].

Results and Discussion

Zero-field magnetic phase transition driven by gate-controlled carrier doping

CrSBr is an air-stable A-type vdW AFM semiconductor with a band gap of ~1.5 eV[27,28] and a high Neel temperature T_N of ~132 K[22,29,30]. It exhibits intralayer FM ordering and AFM interlayer coupling, with the easy axis oriented along the *b*-direction (Fig. 1a)[22,27,31]. Previous attempts to modulate magnetism in CrSBr using conventional solid dielectrics have induced only modest changes in the coercive field of thin flakes[16], while effective gate control in thicker flakes remains even more challenging. More recently, chemical lithium intercalation has been shown to induce an AFM-to-FM phase transition in bulk CrSBr[32], highlighting the critical role of carrier doping in tuning its magnetic ground state. Here, we employ an electrically controlled ionic-liquid gating approach that enables reversible, high-density carrier accumulation and continuous control of the magnetic phase transition in CrSBr flakes, allowing systematic mapping of the phase diagram under electrostatic modulation.

As illustrated in Fig. 2a, we first used $LiClO_4$/PEO electrolyte as the ionic medium in our device (see Methods). The lithium intercalation was controlled by a liquid-gate voltage (V_{LG}) to enable global carrier doping, monitored via room-temperature conductance measurements on a thick CrSBr device (~ 6 nm, Sample D1). At $V_{LG} = 6$ V, the conductivity increases by over an order of magnitude (Fig. 2b). Pristine CrSBr exhibits semiconducting behavior, with conductance decreasing upon cooling and showing a local maximum near 132 K at $V_{LG} = 0$ V (Fig. 2c). This maximum coincides with the onset of AFM ordering and is attributed to the associated suppression of spin-disorder scattering[22]. Upon intercalation doping ($V_{LG} = 6$ V), the conductance

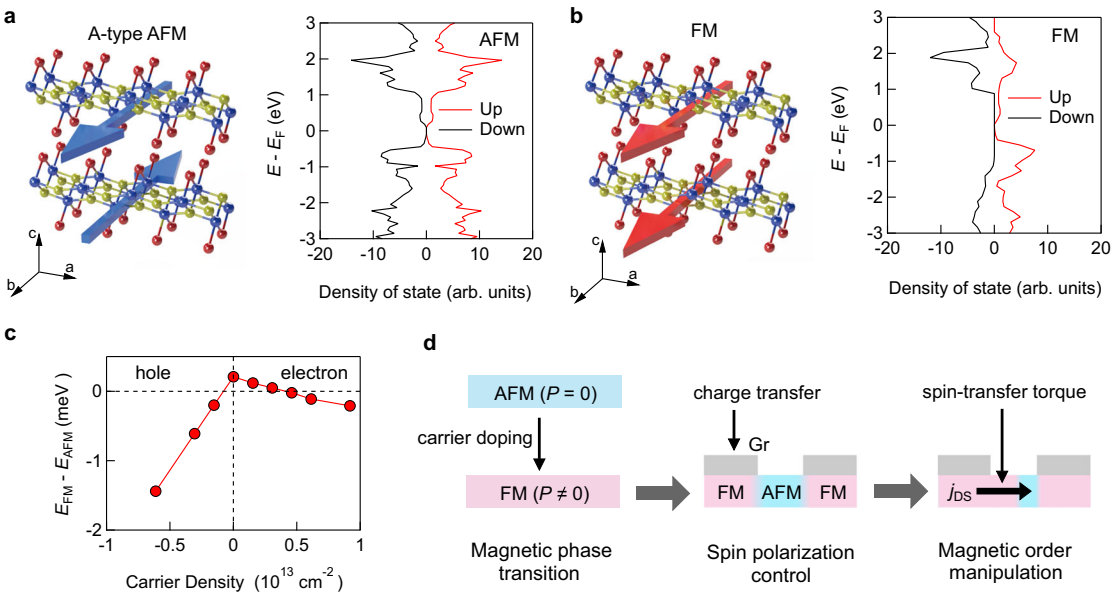

Fig. 1 | Doping-induced magnetic phase transition and spin polarization asymmetry in CrSBr revealed by theoretical calculations. a Schematic illustration of the layered A-type AFM state of CrSBr and corresponding spin-resolved DOS, exhibiting spin degeneracy ($P = 0$). **b** Schematic illustration of the layered FM state of CrSBr and corresponding spin-resolved DOS, showing spin asymmetry ($P \neq 0$), which enables spin-polarized transport and tunable spin polarization. **c** Energy difference between the FM and AFM phases for trilayer CrSBr as a function of doping concentration, indicating that both electron and hole doping can induce the AFM-to-FM phase transition. **d** Our experimental strategy to enable electrical control of magnetic order and spin polarization in CrSBr: First, global carrier doping realizes a zero-field AFM-to-FM phase transition in CrSBr. Second, local doping by interfacial charge transfer from graphene induces confined magnetic order modulation, creating lateral spin-valve configurations with gate-tunable spin polarization. Third, ultralow-current spin-transfer torque manipulates the magnetic order in the CrSBr channel.

https://doi.org/10.1038/s41467-025-67561-3

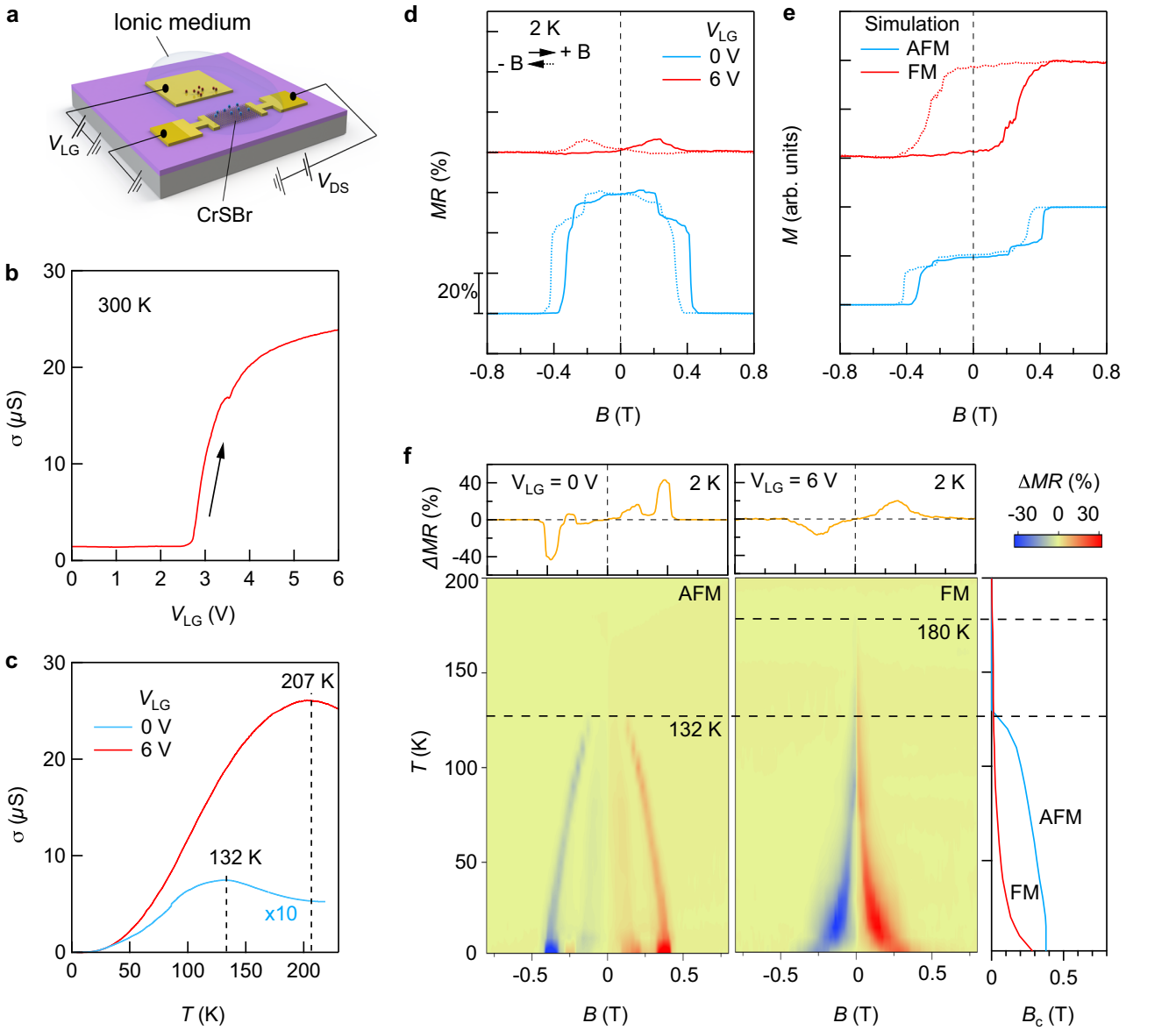

Fig. 2 | Zero-field AFM-to-FM phase transition in CrSBr induced by carrier doping. a Schematic of the device structure by ionic gating. The ionic media $LiClO_4$/PEO is chosen for global intercalation doping. **b** Conductance versus gate for a thick CrSBr device (Sample D1) at 300 K, showing more than one order of magnitude increase in conductivity after 6 V intercalation. **c** Temperature-dependent conductance at 0 V and 6 V, revealing a 75 K shift of the characteristic local maximum from the original Néel temperature (132 K). **d** MR measured at 2 K, where undoped state (0 V) shows AFM -like behavior and doped state (6 V) exhibits FM-like hysteresis, with zero-field resistance matching that at 1 T. **e** Magnetization (*M*) curves extracted from the MR data using micromagnetic simulations, confirming AFM (0 V) and FM (6 V) states. **f** Left and middle panels: MR difference *ΔMR* as functions of temperature and magnetic field for AFM and FM states, revealing a Néel temperature of ~132 K for AFM and a Curie temperature above 180 K for FM. Right panel: Coercive field (B_c) evolution with temperature, highlighting distinct thermal behaviors of the AFM and FM states.

maximum shifts to ~207 K, in consistent with earlier report[32]. In FM semiconductors, T_C typically lies slightly above the conductance maximum[33,34], as seen for monolayer CrSBr[22]. These results indicate that gate-controlled intercalation doping enables effective tuning of the magnetic phase and also increases the magnetic ordering temperatures.

To further verify this magnetic transition, we performed the MR measurements with the external magnetic field (B) sweeping along the easy axis (b-direction) at different liquid-gate voltages and temperatures. The systematic evolution of MR is provided in Supplementary Fig. S3. We define the relative MR as $MR\% = \frac{R(B)-R(0T)}{R(0T)} \times 100\%$. As shown in Fig. 2d, the MR at $V_{LG} = 0$ V primarily decreases sharply at a coercive field of ~ 0.4 T, consistent with a field-induced FM transition superimposed on an AFM ground state, where antiparallel interlayer spins suppress electron hopping. In contrast, following intercalation at 6 V, the AFM signature vanishes, and the MR exhibits a butterfly-shaped hysteresis with zero-field resistance matching that at 1 T, indicating the formation of a stable FM ground state with the magnetic easy axis preserved along b-direction[21,32]. These changes underscore the strong sensitivity of MR to the underlying magnetic structure[22,31,35]. The gate-dependent MR features thus provide direct evidence for an AFM-to-FM transition driven by intercalation-induced carrier doping. Due to the in-plane spin orientation and pronounced transport anisotropy in CrSBr, direct Hall measurements to extract magnetization were not feasible[27,29,30]. Instead, as shown in Fig. 2e, micromagnetic simulations fitted to our MR data (also see Supplementary Note 2 and Supplementary Fig. S4) confirm the AFM and FM behaviors. Furthermore, temperature-dependent MR difference measurements

https://doi.org/10.1038/s41467-025-67561-3

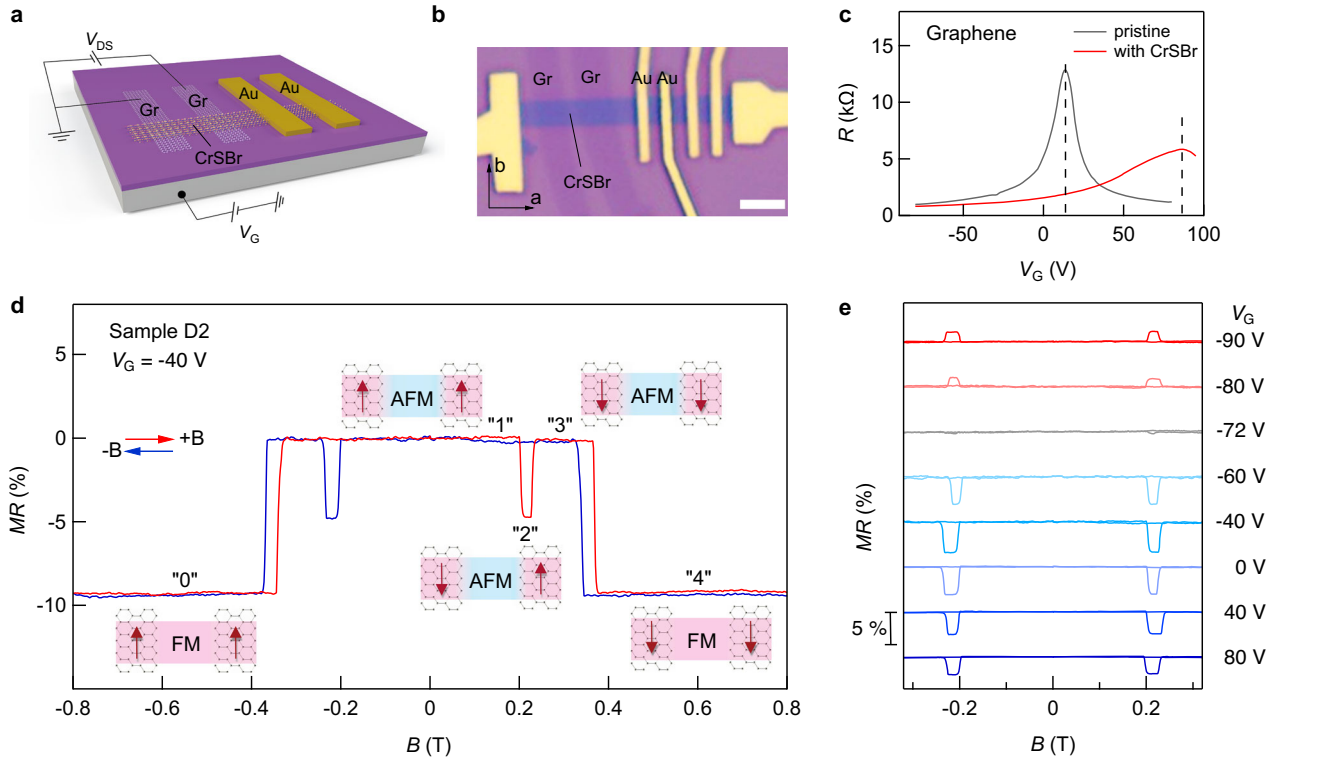

Fig. 3 | Gate-tunable lateral spin valve in CrSBr induced by local interfacial charge transfer from graphene. a Schematic of the CrSBr lateral spin-valve with graphene contacts on a 285 nm SiO_2/Si substrate. The global back-gate voltage V_G is applied to the doped Si substrate; V_{DS} is applied between the graphene source and drain electrodes. **b** Optical image of a trilayer CrSBr device with graphene contacts (Sample D2). Scale bar: 5 µm. **c** Transfer curves of the pristine graphene and graphene in contact with the CrSBr flake in Sample D2 measured at 2 K. **d** MR of the same CrSBr device measured with V_{DS} = 0.48 V and V_G = - 40 V at 2 K. The inset cartoons illustrate the corresponding magnetic configurations for resistance states "0" to "4" as the magnetic field sweeps forward (red curve) along the b-axis. The coercive field of the source Gr/CrSBr contact slightly differs from that of the drain contact, forming parallel (state "1" or "3") and antiparallel (state "2") magnetic configurations as the field sweeps, thus causing the spin-valve effect. **e** Spin-valve MR of the same device as V_G changes from - 90 V to 80 V with a fixed V_{DS} = 0.48 V, at 2 K with magnetic field B oriented along the b-axis. It clearly shows a sign change of the spin-valve MR when adjusting V_G across - 72 V.

(defined as $\Delta MR = MR_{forward}\% - MR_{backward}\%$) reveal distinct thermal evolutions of the coercive field (B_c) and an enhanced critical temperature (T_C) for the AFM and FM states (Fig. 2f). As the magnitude of interlayer exchange coupling is smaller than intralayer ones by about two orders of magnitude (see Supplementary Note 3 and Supplementary Table S2), this increase in T_C primarily arises from electron-doping-enhanced intralayer effective exchange interactions in CrSBr as supported by our first-principles calculations (Supplementary Figs. S5, S6), underscoring the effective thermal stabilization of FM order through carrier doping[32].

Local magnetic order modulation and gate-controlled spin-valve behavior

Having confirmed carrier doping as the mechanism for modulating the magnetic order in CrSBr, we next employ the local-doping strategy that exploits interfacial charge transfer from graphene to spatially modulate the magnetic order of pristine CrSBr. This approach enables spin injection and detection through separated doping-induced FM regions and the resulting spin-filtering effect. Figure 3a, b show the schematic and optical image of our CrSBr/Gr heterostructure device (Sample D2), where two graphene stripes serve as electrodes and the global back-gate voltage V_G is applied to the doped Si substrate. The CrSBr flake is identified as a trilayer based on optical contrast and atomic force microscopy (Methods, Supplementary Fig. S1), with a channel length of ~1 µm along the a-axis. Theoretical studies predict strong charge transfer at the CrSBr/Gr interface, leading to effective electron doping capable of inducing an AFM-to-FM transition in thin-layer CrSBr[21] (also see Fig. 1c). To verify this in our device, we compared the transfer curves of pristine graphene with graphene in contact with CrSBr, as shown in Fig. 3c. The CrSBr/Gr interface induces a 73 V shift in graphene's charge neutrality point, corresponding to a large charge transfer of ~ 5.5×10^{12} cm^{-2} (calculated from the 285 nm SiO_2 gate capacitance and typically required high quality interface between graphene and CrSBr). This substantial charge transfer is sufficient to locally induce FM order[21] at the two graphene-contacted regions, creating a lateral FM/AFM/FM configuration that supports a spin-valve effect for verifying spin polarization modulation.

To demonstrate the resulting spin-valve behavior, we performed magneto-transport measurements at 2 K. Figure 3d presents the MR data measured using two graphene contacts under a bias voltage of V_{DS} = 0.48 V and a gate voltage V_G = - 40 V. During the magnetic field sweeps, an MR transition appears at a coercive field of ~ ± 0.35 T, labeled "AFM MR", indicating spin flipping in the CrSBr channel from an AFM to an FM state[22,27,36]. Within the high-resistance plateau of the AFM ordering, abrupt drops in resistance occur near ± 0.2 T, depending on the sweep direction. These hysteretic drops are characteristic of spin-valve behavior[28,37] (denoted as "spin-valve MR") in our CrSBr device with graphene contacts. In the inset of Fig. 3d, we label discrete resistance states "0" to "4" and illustrate the corresponding magnetic states for the forward sweep of magnetic field (red curve). The associated spin configurations in the CrSBr layers are discussed in Supplementary Note 4 and Supplementary Fig. S7. We note that the spin-valve behavior is also reproducible when the field sweep is confined within ± 0.3 T (Supplementary Fig. S7b). Finally, control experiments using Au-Au and Gr-Au contacts (Supplementary Fig. S8) do not exhibit similar spin-valve MR, confirming that the observed spin-valve

https://doi.org/10.1038/s41467-025-67561-3

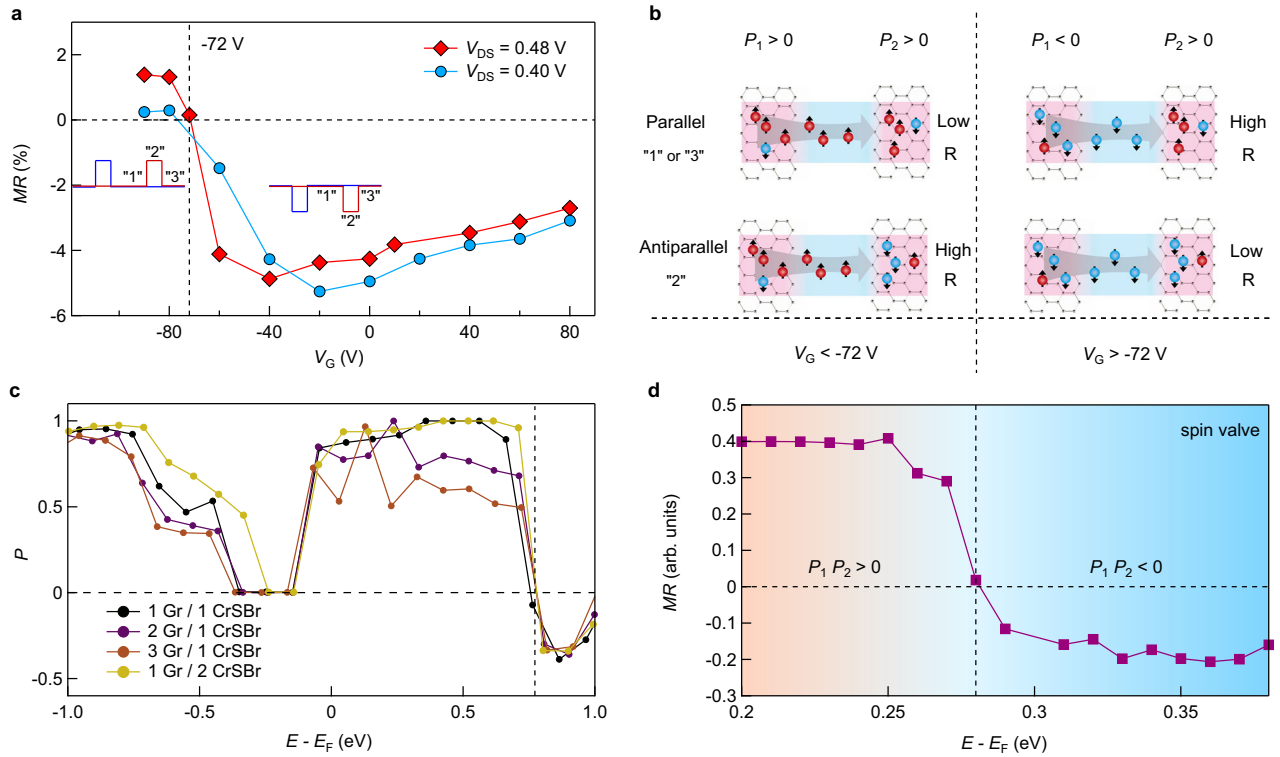

Fig. 4 | Gate-controlled spin-polarization reversal in the CrSBr spin valve. **a** Spin-valve MR (extracted from Fig. 3d and Supplementary Fig. S8 for Sample D2) as a function of V_G for V_{DS} = 0.48 V and 0.40 V, respectively. **b** Illustration of the MR states depending on spin polarization and magnetic configurations of the CrSBr/Gr contacts. $P_1 > 0$ and $P_2 > 0$ at $V_G < -72$ V, so the matched spin channels in the parallel configuration (state "1" or "3") lead to a low-resistance (R) state. Conversely, it exhibits a higher resistance in the antiparallel configuration (state "2"). The situation reverses when $P_1 < 0$ and $P_2 > 0$ at $V_G > -72$ V with the same bias. **c** Calculated spin polarization P of DOS as a function of energy for CrSBr/Gr heterostructures with various layer thicknesses, including one layer of CrSBr and one layer of graphene (1 CrSBr/1 Gr), 1 CrSBr/2 Gr, 1 CrSBr/3 Gr, and 2 CrSBr/3 Gr. The spin polarization is nearly insensitive to the thickness of all these heterostructures. **d** Calculated spin-valve MR under an AC bias of V_{DS} = 0.48 V. The sign of spin valve MR is determined by the spin polarization product (P_1P_2) of two CrSBr/Gr contacts. The vertical dashed line marks the MR sign reversal at E = 0.28 eV, quantitatively matching with experimental results and confirming gate-controlled spin polarization reversal.

behavior arises intrinsically from the lateral configuration created by local charge transfer from graphene. More discussion is provided in Supplementary Note 5 and Fig. S9.

More importantly, this spin-valve behavior is fully gate-tunable, featuring a sign reversal of the spin-valve MR that confirms electrical control of the spin polarization in our CrSBr device. We performed MR measurements at different gate voltages over a magnetic field sweep of ± 1 T (Supplementary Fig. S10) and the central ± 0.3 T window is shown in Fig. 3e. At a fixed V_{DS} = 0.48 V, positive spin-valve MR is observed at V_G = - 90 and - 80 V, followed by complete suppression at a critical gate bias of V_G = - 72 V. Adjusting V_G across the critical point restores the spin-valve MR with a reversed sign as V_G is increased from −90 to 80 V. Similar gate tunability is observed at V_{DS} = 0.4 V (Supplementary Fig. S11). In another CrSBr device (Sample D3) that is encapsulated with hBN and equipped with a high-k dielectric, the gate tunability is further enhanced, allowing the positive spin-valve MR to be modulated from 36% to nearly zero by increasing V_G from -2 to 0 V (Supplementary Fig. S12). Such robust gate control represents a significant advance over the conventional spin-valve devices that rely on FM metal contacts[24].

Gate-tunable spin polarization in CrSBr/Gr heterostructure

We attribute the sign reversal of the spin-valve MR near V_G = −72 V (Fig. 4a) to the gate-tunable spin polarization of the two CrSBr/Gr electrodes under a large bias. The spin polarization of each electrode is determined by the distribution of spin-resolved electronic states within the transport energy window defined by its local electrochemical potential. Under a finite bias V_{DS}, these transport windows are offset between the two contacts and can be rigidly shifted together by the global gate V_G, as illustrated in Supplementary Fig. S13. When the dominant spin species within the respective energy windows differ, the two electrodes acquire opposite spin polarization. As illustrated in Fig. 4b, the net spin polarization of each CrSBr/Gr electrode thus depends jointly on V_{DS} and V_G. When $V_G < -72$ V, both electrodes exhibit positive spin polarization (left panel of Fig. 4b), resulting in a low-resistance state for the parallel alignment of their magnetizations (states "1" or "3"), and a high-resistance state for the antiparallel alignment (state "2"). Once V_G exceeds the critical bias, the electrodes acquire opposite spin polarizations (right panel of Fig. 4b), inverting the resistance state. Consequently, the sign of the spin-valve MR is determined by the product of the spin polarization of two electrodes (P_1 and P_2), assuming that spin polarization remains unchanged during spin diffusion through the channel.

To further elucidate this behavior, we calculated the spin polarization P for the CrSBr/Gr heterostructures with various layer thicknesses using density functional theory (Fig. 4c). The corresponding band structures for different CrSBr/Gr configurations are shown in Supplementary Note 6 and Supplementary Fig. S14. These calculations reveal that the spin polarization is nearly insensitive to the thickness of graphene or CrSBr, highlighting its robustness across a wide range of device parameters. Figure 4d presents the calculated MR, which scales with $P_1P_2 = P(E)[P(E + eV_{DS}) + P(E - eV_{DS})]/2$, where V_{DS} = 0.48 V is the AC bias between the two CrSBr/Gr electrodes, and E is the electrochemical potential of the drain-side CrSBr/Gr electrode. The gate

https://doi.org/10.1038/s41467-025-67561-3

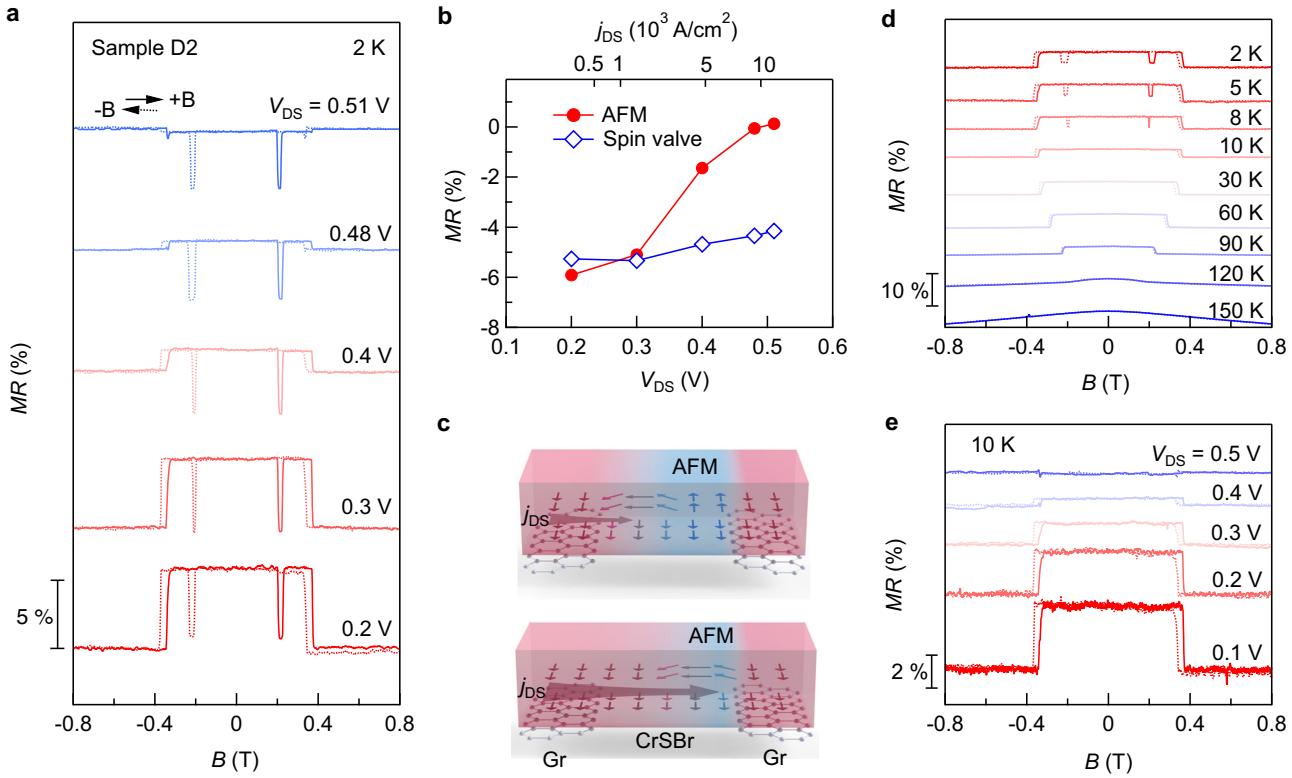

Fig. 5 | Electrical manipulation of magnetic order in the lateral CrSBr channel. **a** Bias voltage (V_{DS})-dependent MR of the CrSBr device (Sample D2) measured at 2 K with a fixed V_G = 0 V. The AFM MR diminishes while the spin-valve MR persists as V_{DS} increases, indicative of the STT effect within the CrSBr channel. **b** The AFM MR and the spin-valve MR as a function of V_{DS}, with the top axis representing the corresponding source-drain current density j_{DS}. **c** Schematic of STT-driven magnetic order manipulation in the lateral CrSBr channel for small (top) and large (bottom) j_{DS}. The intensified spin current enhances STT effects, switching the CrSBr channel from initial AFM order (blue region) to the FM order (red region). **d** MR of the same device measured at various temperatures from 2 K to 150 K with V_{DS} = 0.2 V and V_G = 0 V, illustrating the disappearance of the spin-valve MR near 10 K. **e** Bias voltage-dependent MR of the same device measured at 10 K with V_G = 0 V. The AFM MR decreases with increasing V_{DS}, further supporting the presence of the STT effect at elevated temperatures.

voltage simultaneously shifts the Fermi levels of both electrodes, leading to a sign reversal in calculated MR when the Fermi level moves to ~ 0.28 eV (dashed line in Fig. 4d). By estimating the carrier density in graphene under these conditions, we find excellent quantitative agreement with the experimental data (Fig. 3c), where the spin-valve MR sign reverses at VG = - 72 V(Supplementary Note 7). This result confirms that the gate modulation can fully reverse the spin polarization in our CrSBr spin-valve device, demonstrating large tunability.

Electrical manipulation of magnetic order through STT

We also observe a pronounced STT effect in the lateral CrSBr channel, enabled by large spin-polarized current injected through doping-induced FM contact regions. STT transfers spin angular momentum, thereby altering the magnetic order of the CrSBr channel. To confirm this, we measured the MR at 2 K over a range of V_{DS}, as shown in Fig. 5a. With V_G = 0 V, the current increases nonlinearly from 18 to 856 nA as V_{DS} is raised from 0.2 to 0.51 V, while the spin-valve MR remains nearly constant. In contrast, the AFM MR gradually diminishes and eventually vanishes at higher V_{DS}.

Figure 5b presents the evolution of the AFM and spin-valve MR with V_{DS}. Theoretical calculations indicate that the spin polarization of CrSBr/Gr heterostructure remains nearly unchanged over this bias range (Supplementary Fig. S15). Hence, we attribute the disappearance of the AFM MR to the increased spin current density, which amplifies the STT in the channel and drives an AFM-to-FM magnetic order switching (Fig. 5c). As expected, adjusting the DC bias voltage can also modulate the magnetic state via STT, as confirmed in Samples D2 (Supplementary Fig. S16) and D3 (Supplementary Fig. S17). To validate this STT mechanism, we performed control experiments on CrSBr devices with Au electrodes (Supplementary Fig. S18). Increasing the current in these devices does not suppress the AFM MR, confirming that the STT effect is unique to our device configuration with graphene contacts. Such STT-driven magnetic order manipulation is rarely observed in lateral spin-transport devices using two-dimensional (2D) magnetic materials or thin magnetic films[38,39].

We estimate that the threshold current density (j_{DS}) required to induce STT in our devices is less than 10^3 A/cm^2 (top axis of Fig. 5b, also see Supplementary Note 8 and Table S1), which is more than an order of magnitude lower than previously reported spin-torque thresholds in lateral structures[38,40]. This reduction likely stems from the clean vdW interfaces in our heterostructures, which minimize pinning centers relative to conventional FM-metal interfaces. Recent reports of layer-sharing lateral exchange bias effect in CrSBr also support our scenario of low current STT[41].

We further explored the temperature dependence of the MR at V_{DS} = 0.2 V and V_G = 0 V from 2 to 150 K (Fig. 5d). The AFM coercive field decreases as the temperature is increased, and the AFM MR persists up to ~ 130 K, consistent with previous reports[22,27,29,31]. In contrast, the spin-valve MR vanishes near 10 K, presumably due to a reduced spin diffusion length at elevated temperatures. As shown in Fig. 5e, the AFM MR decreases whereas the coercive field remains unchanged with increasing V_{DS} at 10 K, confirming that STT effects persist at elevated temperatures and ruling out purely thermal influences. Meanwhile, the emergence of positive MR in perpendicular fields and butterfly-shaped MR signals with parallel fields at higher V_{DS} (Supplementary Fig. S9c and Fig. S19) further supports an STT-induced FM order. Similar butterfly-shaped MR signals also appear on the high-

resistance AFM plateau when the temperature exceeds 10 K (Supplementary Fig. S20), indicating the coexistence of FM and AFM order[42] in the CrSBr. This temperature-dependent spin-valve and MR behavior is likewise observed in a four-layer CrSBr device with graphene electrodes (Sample D4, Supplementary Fig. S21), underscoring the versatility and effectiveness of our approach for realizing gate-tunable lateral spin valves without conventional FM contacts.

In summary, we demonstrate that carrier doping serves as an effective and versatile mechanism for controlling both magnetic order and spin polarization in a single vdW antiferromagnet, CrSBr. By leveraging the strong coupling between charge density and interlayer exchange interactions, we achieve a deterministic and reversible AFM-to-FM phase transition at zero magnetic field. Complementary approaches of interfacial charge transfer and STT enable spatial and dynamic modulation of magnetic states, expanding the tunability of this system. Notably, we realize lateral spin-valve configurations with gate-controlled spin polarization reversal and large tunability, all without relying on FM contacts. Furthermore, the low current densities ($<10^3$ A/cm^2) required for STT-driven switching point to the potential for energy-efficient spintronic operation. Together, these findings highlight CrSBr as a promising model system for all-electrical spintronic devices, integrating multiple spin functionalities within a single gate-tunable material.

Methods

Sample growth and device fabrication

High-quality CrSBr single crystals were successfully synthesized via the chemical vapor transfer (CVT) method, using high-purity chromium metal powder, sublimated sulfur powder, and liquid bromine as precursors. The growth conditions and steps are described in detail in Supplementary Note 1. We used a polydimethylsiloxane (PDMS) stamp-assisted mechanical exfoliation technique to prepare CrSBr thin flakes in air. The layer number of the flakes was determined by height profiling using an atomic force microscope and observing optical contrast in optical micrographs (Supplementary Fig. S1).

CrSBr devices with graphene contacts were fabricated using a PC-based dry- transfer technique[43]. To ensure high-quality, bubble-free CrSBr/Gr interfaces, we adopted an additional thermal expansion-contraction control step during the transfer process. The PC film was heated to 150 °C for adhesion and slowly cooled to 60 °C for controlled release, while repeated mild thermal cycles during the drop-down process eliminated trapped bubbles. Finally, the PC layer was dissolved in trichloromethane to obtain a clean, residue-free interface. Typical CrSBr flakes are in a ribbon shape, with long and short edges corresponding to the *a* and *b* crystal axes, respectively. The CrSBr thin flakes were stacked onto the graphene electrodes on 285 nm SiO_2/Si substrates with long edges aligned vertically to the graphene stripes. Subsequently, Cr/Au (5/70 nm) electrodes were defined and thermally evaporated onto CrSBr or graphene using a standard electron-beam lithography process.

Electrical transport measurements

The ionic medium $LiClO_4$/PEO polymer electrolyte was applied to the top of the thin flake and the side gate electrode for ionic gating. The device configuration is illustrated in Fig. 2a. $LiClO_4$ and PEO powders (0.3 g and 1 g, respectively) (PEO; M_w = 100,000) were mixed with 15 ml anhydrous methanol (Alfa Aesar). The mixture was then stirred overnight with the temperature kept at 50 °C[44]. The global intercalation doping is controlled by adjusting the gate voltage and its doping effect is monitored by measuring the conductivity of the CrSBr device at room temperature.

Low-temperature transport measurements down to 2 K were performed in a commercial Cryogenic Superconducting Magnet System (1.6–300 K, 12 T). Longitudinal resistance was measured in a two-terminal configuration, using an SR830 lock-in amplifier combined with an SR570 current amplifier for sourcing voltage and measuring current at a reference frequency of 17.77 Hz. For DC measurements, a Keithley 2636 A was used to source voltage and measure current. Gate-dependent measurements were conducted using a Keithley 2400 to apply voltages to the gates.

Theoretical calculations

We performed density functional theory (DFT) calculations, implemented in the Vienna Ab initio Simulation Package (VASP)[45], to determine the carrier-doping-dependent energy difference between collinear FM and AFM states of CrSBr, as well as the electronic structure of the CrSBr/Gr heterostructures. The projector-augmented wave (PAW) method[46] was employed to describe the interaction between ions and electrons. The Perdew-Burke-Ernzerhof (PBE) functional within the generalized gradient approximation (GGA)[47] was used to treat the exchange-correlation effects. Further details of the theoretical calculations are provided in Supplementary Note 5. We also verified that including the vdW interactions produces negligible changes in the calculated results presented here.

The magnetic properties of CrSBr under carrier doping were systematically investigated through a combination of experimental measurements and computational modeling. Magnetization curves were reconstructed from MR data using established anisotropic magnetoresistance (AMR) and giant magnetoresistance (GMR) frameworks, providing a non-destructive approach to quantitatively track the evolution of magnetization under different magnetic fields. To complement our experiments, we performed Monte Carlo simulations of the CrSBr system using an extended Heisenberg Hamiltonian that incorporates both intralayer and interlayer exchange interactions[35]. The experimental and computational results demonstrated consistent results of magnetization curves. Further details of these theoretical calculations are provided in Supplementary Note 5 and Fig. S2.

Data availability

The Source Data underlying the figures of this study are available at https://doi.org/10.6084/m9.figshare.30630737. All raw data generated during the current study are available from the corresponding authors upon request.

References

1. Žutić, I., Fabian, J. & Das Sarma, S. Spintronics: fundamentals and applications. *Rev. Mod. Phys.* **76**, 323–410 (2004).
2. Datta, S. & Das, B. Electronic analog of the electro-optic modulator. *Appl. Phys. Lett.* **56**, 665–667 (1990).
3. Chuang, P. et al. All-electric all-semiconductor spin field-effect transistors. *Nat. Nanotechnol.* **10**, 35–39 (2015).
4. Datta, S., Salahuddin, S. & Behin-Aein, B. Non-volatile spin switch for boolean and non-boolean logic. *Appl. Phys. Lett.* **101**, 252411 (2012).
5. Huang, B. et al. Layer-dependent ferromagnetism in a van der Waals crystal down to the monolayer limit. *Nature* **546**, 270–273 (2017).
6. Gong, C. et al. Discovery of intrinsic ferromagnetism in two-dimensional van der Waals crystals. *Nature* **546**, 265–269 (2017).
7. Yang, H. et al. Two-dimensional materials prospects for non-volatile spintronic memories. *Nature* **606**, 663–673 (2022).
8. Deng, Y. et al. Gate-tunable room-temperature ferromagnetism in two-dimensional Fe3GeTe2. *Nature* **563**, 94–99 (2018).
9. Jiang, S., Li, L., Wang, Z., Mak, K. F. & Shan, J. Controlling magnetism in 2D CrI3 by electrostatic doping. *Nat. Nanotech.* **13**, 549–553 (2018).
10. Huang, B. et al. Electrical control of 2D magnetism in bilayer CrI3. *Nat. Nanotechnol.* **13**, 544–548 (2018).

11. Fu, Z. et al. Tunneling current-controlled spin states in few-layer van der Waals magnets. *Nat. Commun.* **15**, 3630 (2024).
12. Jiang, S., Li, L., Wang, Z., Shan, J. & Mak, K. F. Spin tunnel field-effect transistors based on two-dimensional van der Waals heterostructures. *Nat. Electron.* **2**, 159–163 (2019).
13. Yao, F. et al. Switching on and off the spin polarization of the conduction band in antiferromagnetic bilayer transistors. *Nat. Nanotechnol.* **20**, 609–616 (2025).
14. Gong, S. J. et al. Electrically induced 2D half-metallic antiferromagnets and spin field effect transistors. *Proc. Natl. Acad. Sci. USA* **115**, 8511–8516 (2018).
15. Liu, G. & Ke, S.-H. Electronic and transport engineering of A-type antiferromagnets with ferroelectric sandwich structure: toward multistate nonvolatile memory applications. *Nano Lett.* **24**, 10776–10782 (2024).
16. Tabataba-Vakili, F. et al. Doping-control of excitons and magnetism in few-layer CrSBr. *Nat. Commun.* **15**, 4735 (2024).
17. Cenker, J. et al. Reversible strain-induced magnetic phase transition in a van der Waals magnet. *Nat. Nanotechnol.* **17**, 256–261 (2022).
18. Jo, J. et al. Nonvolatile electric control of antiferromagnet CrSBr. *Nano Lett.* **24**, 4471–4477 (2024).
19. Tokura, Y. & Nagaosa, N. Orbital physics in transition-metal oxides. *Science* **288**, 462–468 (2000).
20. Bednorz, J. G. & Müller, K. A. Possible high Tc superconductivity in the Ba–La–Cu–O system. *Eur. Phys. J. B.* **64**, 189–193 (1986).
21. Xie, K., Zhang, X. W., Xiao, D. & Cao, T. Engineering magnetic phases of layered antiferromagnets by interfacial charge transfer. *ACS Nano* **17**, 22684–22690 (2023).
22. Telford, E. J. et al. Coupling between magnetic order and charge transport in a two-dimensional magnetic semiconductor. *Nat. Mater.* **21**, 754–760 (2022).
23. Crooker, S. A. et al. Imaging spin transport in lateral ferromagnet/semiconductor structures. *Science* **309**, 2191–2195 (2005).
24. Tombros, N., Jozsa, C., Popinciuc, M., Jonkman, H. T. & van Wees, B. J. Electronic spin transport and spin precession in single graphene layers at room temperature. *Nature* **448**, 571–574 (2007).
25. Lou, X. et al. Electrical detection of spin transport in lateral ferromagnet–semiconductor devices. *Nat. Phys.* **3**, 197–202 (2007).
26. Koo, H. C. et al. Control of spin precession in a spin-Injected field effect transistor. *Science* **325**, 1515–1518 (2009).
27. Telford, E. J. et al. Layered antiferromagnetism induces large negative magnetoresistance in the van der Waals semiconductor CrSBr. *Adv. Mater.* **32**, e2003240 (2020).
28. Ghiasi, T. S. et al. Electrical and thermal generation of spin currents by magnetic bilayer graphene. *Nat. Nanotechnol.* **16**, 788–794 (2021).
29. Wilson, N. P. et al. Interlayer electronic coupling on demand in a 2D magnetic semiconductor. *Nat. Mater.* **20**, 1657–1662 (2021).
30. Wu, F. et al. Quasi-1D electronic transport in a 2D magnetic semiconductor. *Adv. Mater.* **34**, e2109759 (2022).
31. Boix-Constant, C. et al. Probing the spin dimensionality in single-layer CrSBr van der Waals heterostructures by magneto-transport measurements. *Adv. Mater.* **34**, e2204940 (2022).
32. Feuer, M. L. et al. Charge density wave and ferromagnetism in intercalated CrSBr. *Adv. Mater.* **37**, 2418066 (2025).
33. Alexander, S., Helman, J. S. & Balberg, I. Critical behavior of the electrical resistivity in magnetic systems. *Phys. Rev. B* **13**, 304–315 (1976).
34. Balberg, I. & Helman, J. S. Critical behavior of the resistivity in magneticsystems. II. Below Tc and in the presence of a magnetic field. *Phys. Rev. B* **18**, 303–318 (1978).
35. Boix-Constant, C. et al. Multistep magnetization switching in orthogonally twisted ferromagnetic monolayers. *Nat. Mater.* **23**, 212–218 (2023).
36. Majumdar, P. & Littlewood, P. B. Dependence of magnetoresistivity on charge-carrier density in metallic ferromagnets and doped magnetic semiconductors. *Nature* **395**, 479–481 (1998).
37. Appelbaum, I., Huang, B. & Monsma, D. J. Electronic measurement and control of spin transport in silicon. *Nature* **447**, 295–298 (2007).
38. Wang, Q. et al. Magnetism modulation in $Co_3Sn_2S_2$ by current-assisted domain wall motion. *Nat. Electron.* **6**, 119–125 (2022).
39. Buhl, M. et al. Lateral spin transfer torque induced magnetic switching at room temperature demonstrated by x-ray microscopy. *Sci. Rep.* **3**, 2945 (2013).
40. Fong, X. et al. Spin-transfer torque devices for logic and memory: prospects and perspectives. *IEEE Trans. Comp.-Aided Des. Integr. Circuits Syst.* **35**, 1–22 (2016).
41. Sun, Z. et al. Resolving and routing magnetic polymorphs in a 2D layered antiferromagnet. *Nat. Mater.* **24**, 226–233 (2025).
42. Deng, Y. et al. Quantum anomalous hall effect in intrinsic magnetic topological insulator $MnBi_2Te_4$. *Science* **367**, 895–900 (2020).
43. Lin, Y.-C. et al. Clean transfer of graphene for Isolation and suspension. *ACS Nano* **5**, 2362–2368 (2011).
44. Yu, Y. et al. Gate-tunable phase transitions in thin flakes of 1T-TaS2. *Nat. Nanotechnol.* **10**, 270–276 (2015).
45. Kresse, G. & Furthmüller, J. Efficient iterative schemes for ab initio total-energy calculations using a plane-wave basis set. *Phys. Rev. B* **54**, 11169–11186 (1996).
46. Blöchl, P. E. Projector augmented-wave method. *Phys. Rev. B* **50**, 17953–17979 (1994).
47. Perdew, J. P., Burke, K. & Ernzerhof, M. Generalized gradient approximation made simple. *Phys. Rev. Lett.* **77**, 3865–3868 (1996).

Acknowledgements

We thank Yuanbo Zhang, Mingyuan Huang and Weichao Yu for their helpful discussions. Part of the sample fabrication was performed at the Fudan Nanofabrication Laboratory. This work is supported by the National Key Research and Development Program of China (Grant No. 2024YFB3614103 (W.S.), No. 2024YFA1409003 (W.S.), No. 2021YFA1400400 (J.-W.M.)), the National Natural Science Foundation of China (Grant No. 12574187 (W.S.), No. 12274090 (W.S.), No. 12574115 (Z.Y.), No. 12374101 (Y.L.), No.12474143 (J.-W.M.) and No. 62274087 (J.-W.M.)), the Shenzhen Fundamental Research Program (Grant No. JCYJ20220818100405013 (J.-W.M.) and JCYJ20230807093204010 (J.-W.M.)), Shenzhen Science and Technology Program (Grant No. RCYX20221008092848063 (J.-W.M.)) and Guangdong Provincial Quantum Science Strategic Initiative (GDZX2401010 (J.-W.M.)). J.T.Y. acknowledges the Project TOPCORE (with project number OCENW.GROOT.2019.048) of the research programme Open Competition ENW Groot, which is (partly) financed by the Dutch Research Council (NWO) and the research program 'Materials for the Quantum Age' (QuMat) for financial support. This program (registration number 024.005.006) is part of the Gravitation program financed by the Dutch Ministry of Education, Culture and Science (OCW).

Author contributions

W.S. conceived and supervised the project. Q.L., Y.C., and J.-W.M. grew the CrSBr bulk crystals. G.R.Z., Y.B.Z, K.L.Y., Z.J.G., J.Q.L., and T.Y.Z. fabricated the devices and performed transport measurements. W.S., G.R.Z., Y.B.Z, Z. W., C. Z., J.-W.M., and Z.Y. analyzed the data, Z.Y., Y.L., Y. Z., K.Y., and X.B.C. carried out theoretical calculations. W.S., G.R.Z., J.T.Y., J.-W.M., and Z.Y. wrote the manuscript with input from all authors.

Competing interests

The authors declare no competing interests.

Additional information

Supplementary information The online version contains supplementary material available at https://doi.org/10.1038/s41467-025-67561-3.

Correspondence and requests for materials should be addressed to Jia-Wei Mei, Zhe Yuan or Wu Shi.

Peer review information *Nature Communications* thanks Pritam Deb and the other anonymous reviewer(s) for their contribution to the peer review of this work. A peer review file is available.